Ceramics International xxx (xxxx) xxx

Contents lists available at ScienceDirect

Ceramics International

journal homepage: www.elsevier.com/locate/ceramint

Enhanced photocatalysis via inverse opal structures: Synthesis and characterization of TiO_2/ZnO and ZnO/TiO_2 composites using plasma-enhanced ALD

Hamsasew Hankebo Lemago [a,f,*], Letícia Tolezani [a], Tamás Igricz [c], Dóra Hessz [d,e], Petra Pál [b], Csaba Cserháti [b], Gergő Vecsei [b], Barbara Sárközi [b], Eszter Mónika Baradács [b], Zoltán Erdélyi [b], Imre Miklós Szilágyi [a,**]

[a] Department of Inorganic and Analytical Chemistry, Faculty of Chemical Technology and Biotechnology, Budapest University of Technology and Economics, Műegyetem rkp. 3, H-1111, Budapest, Hungary
[b] Department of Solid-State Physics, Faculty of Sciences and Technology, University of Debrecen, P.O. Box 400, 4002, Debrecen, Hungary
[c] Department of Organic Chemistry and Technology, Faculty of Chemical Technology and Biotechnology, Budapest, University of Technology and Economics, H-1111, Budapest, Hungary
[d] Department of Physical Chemistry and Materials Science, Faculty of Chemical and Bioengineering, Budapest University of Technology and Economics, Műegyetem rkp. 3, H-1111, Budapest, Hungary
[e] Institute of Materials and Environmental Chemistry, Research Centre for Natural Sciences, HUN-REN Research Network, H-1519, Budapest, P.O. Box 286, Hungary
[f] Department of Chemistry, College of Natural and Computational Science, Wachemo University, Hossana, 667, Ethiopia

ARTICLE INFO

Handling Editor: Dr P. Vincenzini

Keywords:
Inverse opals
TiO_2
ZnO
PEALD
Composites
Photocatalysts

ABSTRACT

Inverse opals (IO) based functional materials show potential in photocatalysis due to their unique light interaction properties. This study presents a low-temperature plasma-enhanced atomic layer deposition (PEALD) method for synthesizing TiO_2, ZnO, and composite IOs using a polystyrene nanoparticle-based opal template. We comprehensively characterized the obtained materials using SEM-EDX, TSEM, TG, FTIR, XRD, Raman, ellipsometry, photoluminescence (PL), and UV–Visible spectroscopy. SEM analysis confirmed the successful formation of PEALD IOs with a periodically ordered structure, enabling conformal coating while preserving their original architecture. XRD and Raman analysis also confirmed that the IOs consisted of anatase for TiO_2 and hexagonal wurtzite for ZnO. UV–Vis reflectance spectroscopy revealed strong UV absorption and modified photonic bandgaps (PBGs) for all materials. The bare and composite IOs exhibited PBGs in the visible region, suggesting that the arising "slow photon" effect might enhance photocatalysis. This study explored the photocatalytic degradation of 4-Nitrophenol (4-NP) and Rhodamine 6G (Rh6G) using pristine and composite IO photocatalysts under UV and visible light irradiation. Pristine TiO_2 and ZnO IOs demonstrated superior performance for 4-NP degradation under UV light. This can be attributed to two key factors: their highly ordered macroporous structure (with a large surface area for efficient dye adsorption, and their band gaps (3.0 eV for TiO_2 and 3.2 eV for ZnO) that enable strong absorption of UV light photons for effective pollutant degradation. Conversely, composite IOs (TiO_2/ZnO and ZnO/TiO_2) displayed higher activity for both test molecules under visible light due to a synergistic effect between bandgap harmonization and the PBG effect.

1. Introduction

In the sphere of environmental remediation, photocatalysis shines as a beacon of hope, offering a transformative approach to purifying polluted water and air. Photocatalysts, i.e. extraordinary materials that harness the power of light to trigger electron transfer processes, are key to transforming organic contaminants into harmless byproducts [1]. Among the various photocatalysts, inverse opal (IO) photonic crystals

* Corresponding author. Department of Inorganic and Analytical Chemistry, Faculty of Chemical Technology and Biotechnology, Budapest University of Technology and Economics, Műegyetem rkp. 3, H-1111, Budapest, Hungary.
** Corresponding author.
E-mail addresses: hamsasew.lemago@edu.bme.hu (H.H. Lemago), szilagyi.imre.miklos@vbk.bme.hu (I.M. Szilágyi).

https://doi.org/10.1016/j.ceramint.2024.10.465
Received 2 August 2024; Received in revised form 30 October 2024; Accepted 31 October 2024
Available online 6 November 2024

have emerged as an upcoming class due to their unique optical and structural properties. IOs are engineered marvels, meticulously designed to replicate the hexagonal lattice structure of colloidal crystals [2]. This intricate arrangement of spheres creates a phenomenon known as a photonic band gap (PBG). A PBG is a spectral region where light cannot propagate. The PBG acts like a filter, allowing only specific wavelengths of light to pass through the IOs. This can be tuned to match the light absorption range of the photocatalyst material within the IO photonic crystals. By selectively filtering light, the PBG ensures the catalyst is exposed to photons with the most energy to drive the desired chemical reactions. This targeted light utilization translates to increased efficiency in the photocatalytic process. Furthermore, the PBG can also influence the speed of light travel within the IOs. This is known as the "slow photon" effect. By manipulating the PBG, researchers can trap light for longer inside the IO photonic crystals. This extended light-matter interaction time allows for a greater chance of photons being absorbed by the photocatalyst, further boosting the efficiency of the photocatalytic reactions [3–5].

Opals, known for their striking iridescence, are natural gemstones with a unique internal structure that diffracts light, creating vibrant colors. In contrast, IO PCs are carefully engineered materials that replicate the hexagonal lattice structure of colloidal crystals. The term "inverse opal" refers specifically to a periodic, three-dimensional structure, while the materials used to form this structure can vary, including metals, semiconductors, polymers, and ceramics [6,7]. IO PCs involves a thorough process that begins with synthesizing a colloidal opal crystal template. This template, typically composed of polymer or silica spheres, is arranged in a hexagonal lattice. Next, a precursor material is infiltrated into the template's empty spaces between the nanoparticles, forming a composite structure. Finally, the template is removed, leaving behind an interconnected network of voids, where the walls are filled with the photocatalyst material. The remarkable properties of IOs go beyond just photocatalysis. Their porous structure allows for efficient mass transfer of reactants and products, making them ideal for environmental remediation applications. The exceptional photocatalytic performance is due to the interplay between "slow photon" effects near the PBG edges and the large surface area of IO PCs. By extending the light path within the material, "slow photons" significantly enhance light-matter interaction. This leads to more efficient light utilization and increased generation of reactive species, creating a synergistic effect that paves the way for highly tunable and efficient photocatalysts for various applications [8–11].

TiO_2 and ZnO are widely used photocatalysts due to their attractive properties: low cost, simple synthesis, high chemical stability, and low toxicity. However, TiO_2 has limitations. While it efficiently absorbs light, its activity is restricted to the UV region because of its bandgap (3.2 eV). Additionally, the separation of electron-hole pairs, crucial for photocatalysis, is hampered by TiO_2's low charge carrier mobility [12,13]. In contrast, ZnO exhibits a lower absorption coefficient but a higher electron mobility. This facilitates faster transfer of electrons to the photocatalyst surface, enhancing its activity. However, similar to TiO_2, ZnO also primarily absorbs light in the UV range due to its band gap of 3.4 eV [14,15]. To overcome these limitations, researchers often combine these oxides to obtain TiO_2/ZnO nanocomposites. The similarity between their conduction and valence bands facilitates electron and hole transfer, forming a heterojunction. This heterojunction can narrow the bandgap of TiO_2, allowing it to absorb visible light, and prolong the separation of electron-hole pairs, reducing recombination [16–18]. Furthermore, nanocomposites can significantly enhance photocatalytic activity by introducing defect states within their structure. These defect states, often caused by dopants or non-stoichiometric structures like oxygen vacancies, act as traps for photogenerated electrons or holes. By capturing these charge carriers, they prevent them from recombining and instead promote their participation in pollutant degradation reactions [19–21].

Various techniques are employed to fabricate these composite photocatalysts, including sol-gel, CVD, hydrothermal, electrodeposition, microemulsion, and ALD. Among these, ALD offers precise control over film thickness and morphology, making it a promising method for synthesizing TiO_2/ZnO composites, especially if they are designed as inverse opal photonic crystals [19,20,22–25]. It is a highly precise thin film deposition technique known for its ability to create ultra-conformal films, making it ideal for fabricating complex structures like composite photocatalysts [26]. There are two main types of ALD: thermal ALD and plasma-enhanced ALD (PEALD). Thermal ALD (TALD) relies on heat to activate precursor molecules, while PEALD utilizes plasma (e.g., Ar, H_2, or O_2 radicals for precursor activation) to trigger the reactions. PEALD offers several advantages over thermal ALD for composite photocatalyst fabrication. First, PEALD operates at lower temperatures, which is crucial for integrating materials that might decompose at high temperatures. Second, PEALD excels at depositing highly conformal films with smooth surfaces, which is essential for maximizing the surface area available for photocatalytic reactions. Finally, PEALD provides superior control over film thickness and morphology, allowing for precise tailoring of the composite's photocatalytic properties. However, PEALD also has some drawbacks. While it offers lower deposition temperatures, the films produced might be rougher on a microscopic level and exhibit deviations from the ideal atomic ratio (stoichiometry). Additionally, PEALD precursors might struggle to penetrate deep into the pores of highly porous substrates, resulting in less conformal film growth within those pores [27–31].

Building upon our prior work of synthesizing ZnO IOs coated with Al_2O_3 using thermal ALD (TALD) or PEALD on 600 nm sized PS nanosphere templates, this study addresses the lower photocatalytic degradation efficiency observed in ZnO/Al_2O_3-PEALD composites compared to TALD counterparts. We attribute this to the inherent amorphization caused by the PEALD process [32,33]. Therefore, we focus on synthesizing and characterizing bare TiO_2 and ZnO IOs along with their composites (ZnO/TiO_2 and TiO_2/ZnO) via PEALD at lower temperatures using a 300 nm sacrificial polymer template. These synthesized materials are comprehensively investigated for thermal stability, morphology, composition, structure, crystallinity, and optical properties using a suite of techniques including SEM-EDX, TSEM, TG-DTA, FTIR, XRD, PL, Raman, ellipsometry, and UV–Vis spectroscopy. Finally, their photocatalytic activity is evaluated by monitoring the degradation of rhodamine 6G (Rh6G) and 4-nitrophenol (4-NP) pollutants under UV and visible light irradiation.

2. Experimental procedures

2.1. Preparation of the PS template

To prepare the opal template, we used a 10 % wt, 300 nm PS nanosphere suspension from Sigma Aldrich. The planar substrate was a clean microscope glass slide that had been thoroughly cleaned with soap, ethyl alcohol, and ion exchange water. The glass slide was immersed in piranha (H_2SO_4:H_2O_2 3:1) for 1 h, then dried at 50 °C for 1 h for residue removal & hydrophilicity increase. Next, we prepared the colloidal suspension by adding 4.85 ml of ion-exchange water to 0.15 ml of PS suspension and stirring the mixture thoroughly. The suspension was then placed in a sealable glass container to prevent evaporation. The glass slide was cut to 2.5*3.5 cm and inserted vertically into the as-prepared colloidal suspension (see Fig. 1). The suspension was then placed in a furnace along with a glass of water to promote the formation of a colloidal crystal during the evaporation of water through colloidal self-assembly. The furnace was heated gradually, starting at room temperature, and increasing to 50 °C for 90 min. This temperature was maintained for 14 h to allow for the colloidal self-assembly and successful vertical deposition. Finally, the temperature was raised to 80 °C for 1 h and 30 min, gently evaporating the solvent molecules until the desired colloidal structure was achieved. We have successfully prepared an opal template using this method in our previous studies [33].

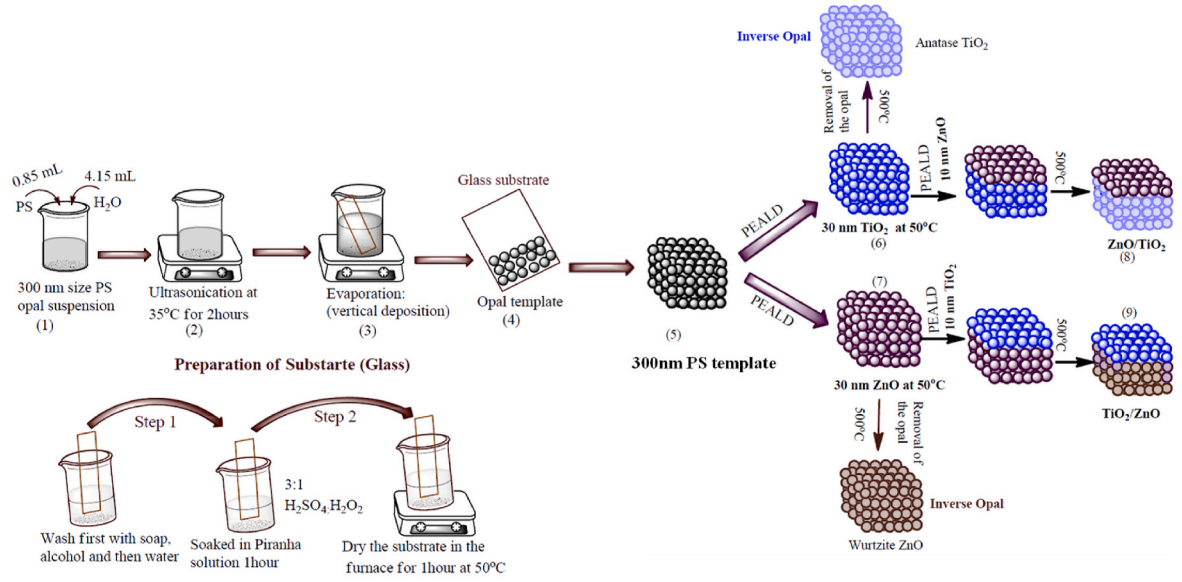

Fig. 1. Schematic representation of the synthesis of TiO_2, ZnO, and composite inverse opals: From PS nanospheres to ordered microporous structures.

2.2. Sample preparation: PEALD

The low-temperature PEALD deposition technique applied plasma species as a co-reactant to enhance precursor reactivity, resulting in the growth of high-quality films. The process commenced with preheating the ALD chamber to 50 °C for 2 h to ensure uniform substrate heating. Subsequently, samples and a reference silicon wafer were inserted into the PEALD reactor to initiate film growth. A consistent 50 W radio frequency power was applied to the plasma during PEALD to activate the O_2 oxidant. Argon served as the carrier gas for delivering oxidant vapor and metallic precursors to the reactor. Internal pressures of 7.4 mBar and 1.2 mBar were maintained within the vacuum chamber and deposition reactor, respectively.

The PEALD process consisted of a sequence of alternating pulses and purges of the reactant gases and an Ar flow, which also served as a purging agent. For TiO_2, the pulse/purge sequence consisted of 0.15 s $TiCl_4$ pulse, 2 s Ar purge, 2 s O_2 plasma exposure, and 2 s Ar purge. This sequence was repeated 286 times, resulting in a 30 nm thick TiO_2 film with a growth rate of 0.10 nm per cycle (GPC). To deposit TiO_2 on ZnO, the pulse/purge program was modified to include DEZ (diethyl zinc) and O_2 precursors. The sequence consisted of 0.3 s DEZ pulse, 3 s Ar purge, 0.3 s O_2 pulse, and 3 s Ar purge. This sequence was repeated 74 times, resulting in a 10 nm thick ZnO film with a growth rate of 0.13 nm GPC. Two samples of ZnO films were also fabricated. The first was deposited using DEZ and water as precursors, following the same pulse/purge sequence as the TiO_2/ZnO film. After 221 cycles, a 30 nm thick ZnO film was obtained, with a growth rate of 0.13 nm GPC. In the second sample, a TiO_2 layer was grown on top of the ZnO using $TiCl_4$ and O_2 as precursors. The pulse/purge sequence for TiO_2 was repeated 96 times, resulting in a 10 nm thick TiO_2 film with a growth rate of 0.10 nm GPC.

Samples were heat-treated in alumina crucibles in a furnace to remove the template material to fabricate IOs. The process involved heating the samples from room temperature to 500 °C for 4 h and then maintaining that temperature for 2 h. The resulting structures consisted of high-quality pristine IOs of TiO_2, ZnO, and their composite (TiO_2/ZnO and ZnO/TiO_2) structures.

2.3. Characterizations

Thermogravimetric (TG) analysis of the PS opal template was conducted using a TA Instruments SDT 2960 device in an air and N_2 atmosphere to determine suitable annealing temperatures for the template and ALD process conditions. The heating rate of 2 °C/min was applied up to 600 °C. The PS sample film was collected in Pt crucibles after being scratched off from the glass slide surface.

Fourier transform infrared (FTIR) spectra of PS opal templates were acquired using a PerkinElmer Spectrum 2000 FT-IR spectrometer at a resolution of 4 cm^{-1}, scanning from 4000 to 400 cm-1. Samples were prepared as KBr pellets and subjected to 64 co-added scans.

The morphology of both the Scanning Electron Microscope (SEM) and Scanning Transmission Electron Microscope (STEM) was analyzed using a SCIOSTM 2 DualBeamTM FIB-SEM (Thermo Fisher Scientific), equipped with an Everhart-Thornley (ET) detector and a field emission gun (FEG) source. This system featured advanced electron optical components, including an annular in-column detector. For STEM analysis, high-angle annular dark-field (HAADF) mode and a STEM + detector were used, with the specimen tilted at 38°. The horizontal field width was set to 1.92 μm. To mitigate charging effects on uncoated samples, a reverse bias of 20 V was applied to the specimen holder.

The EDX analysis was conducted using a JEOL JSM-5500 LV SEM operating at 25 kV. SEM images of the PS template sample were examined without modification. To prevent potential charging, a conductive film of either Au or Pd was deposited on them. The EDX spectra from all ALD samples were utilized for element identification, with three measurement points taken for each sample and the results averaged.

XRD analysis was performed using a PANalytical XPert Pro MPD diffractometer with Cu K_α radiation (2θ range 5-70°, step size 0.025°). The resulting patterns were compared to the ICDD database to identify crystalline phases. The mean size of the crystallites, D, was determined with the Scherrer equation:

$$D = \frac{K\lambda}{\beta\, Cos\, \theta} \tag{1}$$

Where K is the constant, λ is the wavelength of the radiation, β is the full width of diffraction peaks at half-maximum (FWHM), and θ is the angle at which the peak occurs (Bragg angle).

The photonic bandgap (PBG) of the IO materials has been estimated by using a modified Bragg's equation (2), shown below [14,34,35]:

$$\lambda_{-}(\max) = 1.632D\left(n_{avg}^2 - Sin^2\,\theta\right)^{1/2} \tag{2}$$

Where λ_{max} is the wavelength of the photonic band maximum of the

materials, D is the diameter of spheres (would generally be taken as 2r, where r is the sphere radius.), θ is the angle between the incident light and the surface of the sample. The average refractive index n_{avg} of the samples can be calculated using the following equation (3):

$$n_{avg} = f_{ZnO}\, n_{ZnO} + f_{TiO2} n_{TiO2} + (1 - f_{ZnO} - f_{TiO2}) n_{air} \quad (3)$$

Where *f* is the filling factor of the solid sphere. In face-centered cubic structures, spheres occupy about 74 % of the space, with the remaining 26 % residing between specific lattice planes. When alternating layers of TiO_2 and ZnO are deposited, their combined filling factor can be calculated, but adjustments are needed to maintain the total void fraction of 26 %. $n_{PS} = 1.6$, $n_{TiO2} = 2.5$, $n_{ZnO} = 2.0$ and $n_{air} = 1.0$ are the refractive indices of PS, TiO_2, ZnO, and air, respectively.

Using the Tauc relation (Eq (4)) and Kubelka-Munk theory [36], band gap energies (E_g) of IOs TiO_2, ZnO, and their composites were calculated from absorption data (α) and photon energy (hν). For indirect E_g (TiO_2) and direct E_g (ZnO) and their composites, Tauc plots $(\alpha h\nu)^{1/2}$ vs. hν and $(\alpha h\nu)^2$ vs. hν were made (Fig. 6c). The band gap energy was obtained by extrapolating the linear portions of the plots to $(\alpha h\nu)^{1/n} = 0$.

$$(\alpha h\nu)^n = A(h\nu - E_g) \quad (4)$$

Raman spectra were gathered using a Jobin Yvon Labram Raman spectrometer equipped with an Olympus BX41 microscope and a 532 nm Nd-YAG laser. Measurements were collected from 100 to 1800 cm^{-1} with a pixel resolution of 1.4-1.5 cm^{-1} and a spectral resolution of approximately 4 cm^{-1}. Three spectral accumulations were performed.

Spectroscopic ellipsometry (Semilab SE-2000) was used to determine the film thickness of the reference samples. For this, reference Si (100) wafers were also introduced as control samples into the ALD system together with the opal and IO samples.

Optical properties of the samples were studied using the UV–Vis spectroscopy of samples recorded with a UV–Vis spectrometer Avantes AvaSpec-2048 fiber optic spectrometer with an Ava Light DHS light source in the presence of Ava Soft software in both absorbance and reflectance mode.

Photoluminescence (PL) spectra were recorded using an Edinburgh Instruments FS5 spectrofluorometer with a stationary fluorescence setup, featuring an excitation wavelength of 280 nm at room temperature and the inclusion of a long pass glass filter in the emission beam set at a nominal wavelength of 320 nm.

To evaluate the photocatalytic performance of samples, they were subjected to both UV and visible light irradiation while immersed in solutions containing 4-NP and Rh6G pollutants for 4 h. The pH of the 4-NP solution was adjusted to 10.01 pH ± 0.01 using a buffer (Thermo Fisher Scientific). This solution had a maximum absorbance peak at 400 nm. The Rh6G solution exhibited a maximum absorbance peak at 530 nm. Each sample was attached to the walls of a glass vessel using plastic tape to ensure that only the film portion was fully submerged in the dye solutions. Before irradiation, the samples were kept in the dark for half an hour to allow adsorption-desorption equilibrium to be established. At regular intervals of 30 min, 2 ml of the solution was carefully pipetted into a quartz cuvette, and its absorbance was measured using an Avantes fiber optic spectrometer (AvaSpec-2048) equipped with an Ava Light-DHS light source. The photocatalytic decomposition of the pollutants was initiated by exposing the sample solutions to both UV and Visible light irradiation from Osram 18W blacklight and visible lamps 3x3 arranged in a stack configuration. The sample solution was placed in front of the central lamp and maintained at 5 cm to guarantee uniform lighting conditions. This experimental setup enabled the quantification of the photocatalytic activity of the PEALD-grown samples over time, providing insights into their efficiency in degrading 4-NP and Rh6G.

3. Result and discussion

Fig. 1 illustrates the fabrication process of highly ordered IO structures of TiO_2, ZnO, and their composites. A PS template and PEALD techniques were utilized (steps 1–9). First, the glass substrate was coated with the PS suspension, followed by solvent evaporation (steps 1–5). Then, low-temperature PEALD infiltration of TiO_2 or ZnO was performed (steps 6 and 7). Finally, the structure was annealed at 500 °C to form the IOs. For composite materials, an additional hybrid layer was grown using PEALD before the template was removed by heating for further crystallization (steps 8 and 9). This schematic also illustrates the two-step preparation of the glass slides.

3.1. Thermal decomposition and FTIR analysis of PS template

A sacrificial PS template was subjected to controlled heating at a rate of 2 °C/min under both air and N_2 atmospheres to simulate the annealing procedure for template removal and subsequent PEALD steps in sample preparation (Fig. 2a and b). Both environments induced an initial mass loss (2.4 % in N_2 and 1.2 % in air) likely attributable to solvent action. TG curves after this exhibited a single, distinct decomposition stage in both air and N_2 atmospheres. This decomposition occurred between 285 and 367 °C, resulting in a ~95 % mass loss in both cases. After this major decomposition, a final decomposition step took place at 365 °C in N_2 and 400 °C in air. In the air, there was no remaining mass since the organic residue burnt out. These results showed that the opal remained stable during low-temperature PEALD deposition using N_2 carrier gas, while annealing in air at 500 °C was effective for creating an IO nanostructure for PS opal template removal.

FTIR analysis of PS nanospheres revealed the presence of characteristic peaks corresponding to the stretching and bending vibrations of different chemical bonds (Fig. 2c). The peaks at 3017 and 2914 cm^{-1} were attributed to the stretching vibration of C-H bonds in the aromatic groups, while the peak at 2835 cm^{-1} was assigned to the stretching vibration of alkyl C-H bonds. The intense peaks at 1592 and 1492 cm^{-1} originated from the stretching vibration of C=C bonds in the benzene rings. The peak at 1021 cm^{-1} was attributed to the bending vibration of C-H bonds in methyl and methylene groups, and the peak at 755 cm^{-1} was assigned to the bending vibration of C-H bonds in the aromatic rings. These findings corroborate the results of a previous study by Wang et al. [37].

3.2. SEM measurement

3.2.1. Polystyrene template morphology

The colloid crystal templates were typically made up of a suspension of monodispersed colloidal spheres arranged in a regular, periodic lattice due to van der Waals forces [38]. Fig. 3a and b shows that the template consists of periodically ordered opal macrostructures with a diameter of approximately 290 nm (as measured by SEM). These macrostructures were self-assembled via vertical deposition techniques. The opal spheres exhibit a close-packed hexagonal lattice arrangement. These spheres originated from commercially available opal with a nominal diameter of 300 nm. This dense packing of particles imparts unique optical and electronic properties to colloidal crystals.

3.2.2. PEALD IO morphological studies

Polystyrene opal templates were successfully infiltrated with either TiO_2 or ZnO and their composites (TiO_2/ZnO and ZnO/TiO_2) using PEALD at low temperatures. The templates were then removed by thermal annealing at higher temperatures, resulting in self-standing, periodically arranged pure TiO_2 or ZnO IO materials (Fig. 4a, b, and f). SEM analysis (details in Table S3) confirmed that annealing shrank the size of the spheres. The SEM imaging also revealed a highly ordered and periodic arrangement of monodispersed colloidal spheres in the IOs, resembling close-packed (100) planes of a face-centered cubic (FCC) crystal lattice. The IO structures exhibited a honeycomb-like morphology, with voids replacing the spheres in the same lattice. Additionally, SEM revealed the presence of minor cracks in both TiO_2

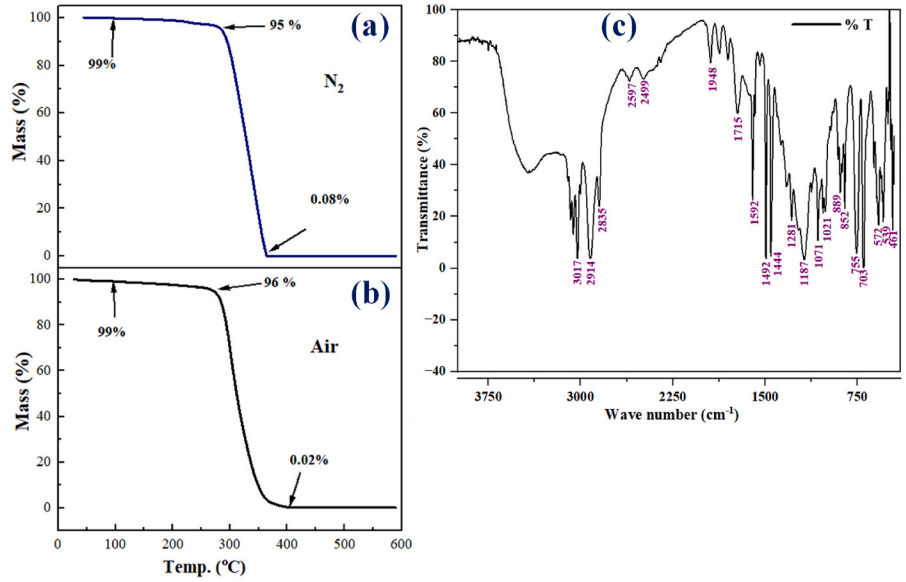

Fig. 2. Thermal analysis of the sample in nitrogen (a) and air (b) environments, and FTIR spectra (c) of PS sacrificial template respectively.

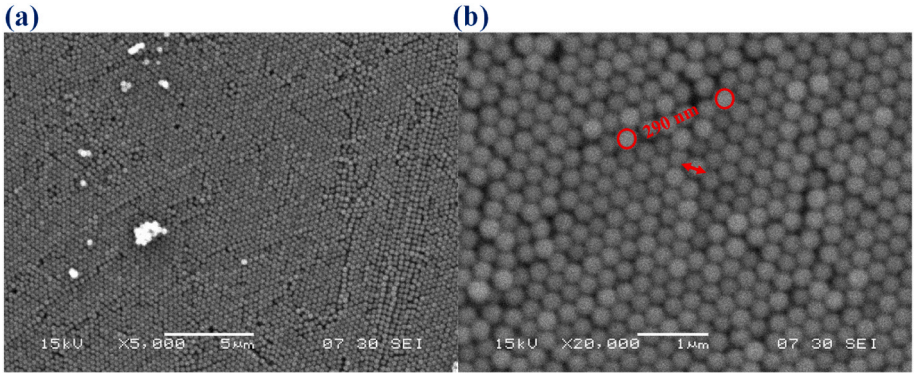

Fig. 3. SEM images of PS sacrificial template made by using vertical deposition method (a and b).

and ZnO IOs (Table S3). SEM measurements also indicated a percentage of shrinkage in TiO_2 (14 %) compared to ZnO IOs (3.4 %) after heat treatment.

SEM analysis showed no significant changes to the overall architecture of the IO after depositing a 10 nm layer of TiO_2 or ZnO onto the existing 30 nm pristine TiO_2 or ZnO layer (Fig. 3c-e, and g & h). The cross-sectional view in Fig. 4h confirms an ordered and periodic pore network, mimicking the original colloidal crystal template. These interconnected pores demonstrate the complete removal of the opal template. Importantly, the thermal annealing process (details in Table S3) resulted in void size shrinkage within the original template, without affecting the morphology of the IO structure itself. These findings highlight the effectiveness of the PEALD technique in depositing a uniform and conformal coating while preserving the original inverse opal architecture.

Moreover, STEM images of composites fabricated with ZnO/TiO_2 and TiO_2/ZnO (Fig. S1) revealed a well-defined periodic lattice of interconnected pores. Ellipsometry measurements suggested a total thickness of 40 nm for both composites, with the ZnO/TiO_2 composite having a 10 nm ZnO layer on a 30 nm TiO_2 layer, and the TiO_2/ZnO composite having a 10 nm TiO_2 layer on a 30 nm ZnO layer. However, STEM analysis indicated slightly different thicknesses. The ZnO/TiO_2 composite had an overall thickness of 29 nm, and the TiO_2/ZnO composite had an overall thickness of 32 nm. This discrepancy can be attributed to the difference in measurement techniques: ellipsometry provides an average thickness based on optical properties, while STEM offers a cross-sectional view. Additionally, the heating process during sample preparation for STEM might have caused minor structural changes. Overall, the STEM also confirmed the successful fabrication of inverse opal composites with precisely controlled layer thicknesses and uniform morphologies.

3.3. EDX measurement

EDX analysis confirmed that TiO_2, ZnO, and their composite materials were successfully deposited using PEALD techniques. As evident in both Table S1 and Fig. S2, the pristine TiO_2 and ZnO IOs and their composites were composed of significant quantities of Ti, Zn, and O atoms, indicating successful ALD oxide formation. EDX analysis further revealed trace amounts of C originating from residual precursors, and traces of Na, Al, Si, and Ca originating from the glass substrate. These impurities were present in minor quantities and did not noticeably impact the properties of the TiO_2 and ZnO materials.

3.4. XRD and crystallite size analysis

Fig. 5a displays the XRD patterns, which exhibit distinct peaks that correspond to the crystal structures of the TiO_2 and ZnO IO crystal structures. The strong pristine TiO_2 IO peaks (25.7°, 38.5°, 48.5°, 54.5°, and 55.6°) confirmed the presence of anatase tetragonal crystal

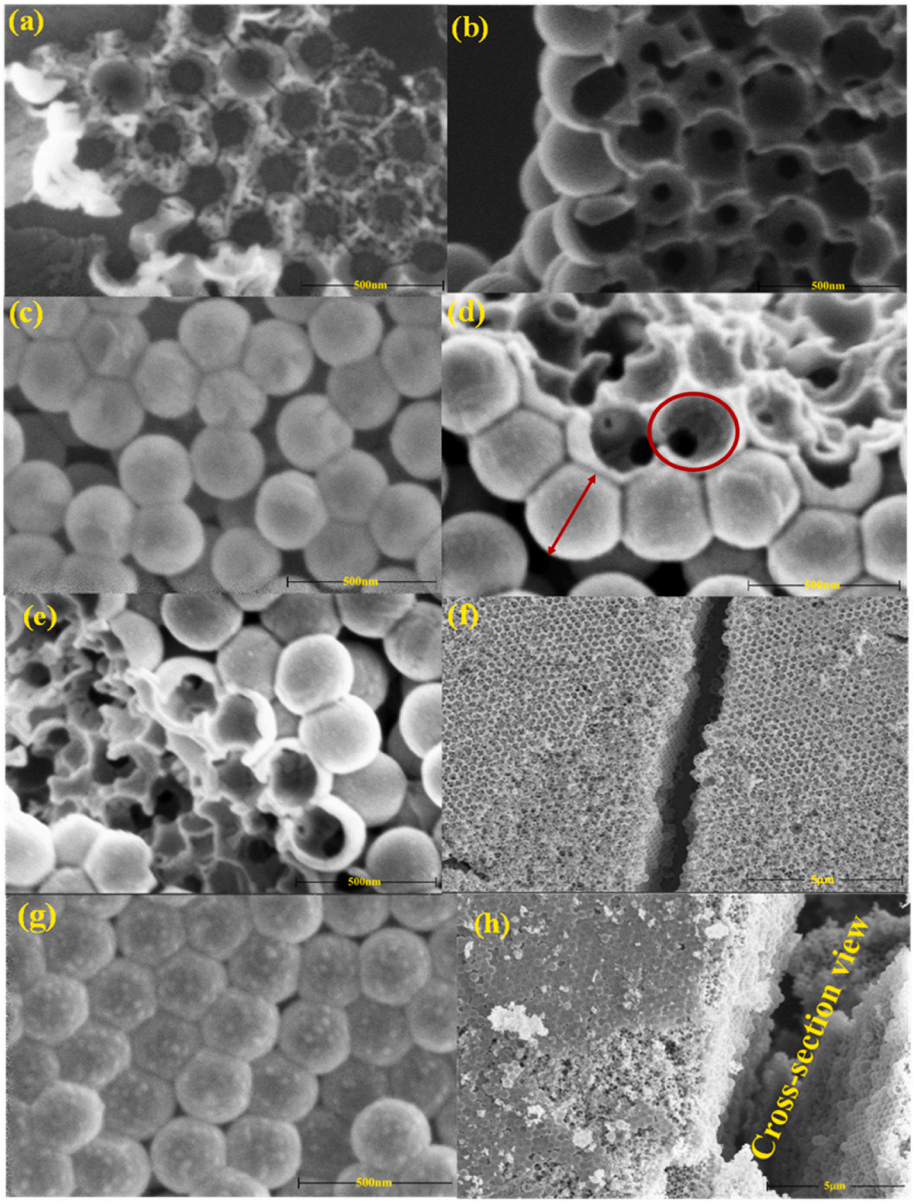

Fig. 4. SEM images of pristine TiO_2 IO (a and b), ZnO on TiO_2 composite, (c-e), pristine ZnO IO (f), and TiO_2 on ZnO composite (g and h) using the PEALD method.

arrangement (ICCD: 98-009-2363), while the pristine ZnO IO peaks (32.5°, 34.8°, 36.6°, 57.2°, 63.2°, and 68.2°) suggested hexagonal wurtzite crystal arrangement (ICCD: 98-015-4489). This observation was attributed to the annealing step, which removed the sacrificial template material. In contrast, the XRD patterns of the composite IOs, consisting of either a 10 nm ALD layer of ZnO on TiO_2 or TiO_2 on ZnO, did not exhibit any detectable peaks for the outer layer. This limitation was due to the thinness of the ALD layer, which was insufficient for effective detection by the equipment.

The average size of individual crystals in pristine TiO_2 IO and its composite material was determined to be 27.6 nm and 27.3 nm, respectively, using the Scherrer equation (Table S2). This size range falls within the typical values for TiO_2, which typically ranges from 20 to 50 nm. Similarly, the crystallite sizes of ZnO IO and ZnO/TiO_2 composite were found to be 26.3 nm and 25.4 nm, respectively, as reported in previous studies [39,40].

The FWHM of the diffraction peaks indicated that both materials possessed relatively defect-free crystal structures. For TiO_2 IO and TiO_2/ZnO, the FWHM values were 0.31 radians and 0.32 radians, respectively. For ZnO IO and ZnO/TiO_2, the FWHM values were 0.33 radians and 0.30 radians, respectively. These findings collectively suggest the successful synthesis of pristine TiO_2 and ZnO IOs and their respective composite nanostructures. The consistent crystallite sizes and narrow FWHM values demonstrate the absence of significant crystal defects, indicating the high quality of these materials [41].

3.5. Raman measurement

The Raman spectroscopy results in Fig. 5b confirm the presence of the anatase phase in the TiO_2 IO samples. The distinct peaks observed correspond to various vibrational modes of the TiO_2 crystal structure. The strongest peak at 142 cm^{-1} is assigned to the E_g mode, which involves the bending vibration of oxygen atoms in the TiO_2 lattice [42]. Additionally, smaller peaks at 197 cm^{-1} (E_g), 393 cm^{-1}(B_{1g}), 516 cm^{-1}(B_{1g}), and 635 cm^{-1} (E_g) are attributed to other vibrational modes of the anatase phase, including the E_g bending and stretching modes of Ti-O bonds, and the B_{1g} stretching mode of O-Ti-O bonds. These characteristic peaks match well with the expected vibrational modes for anatase TiO_2, signifying the absence of other phases like rutile in the synthesized samples [43,44].

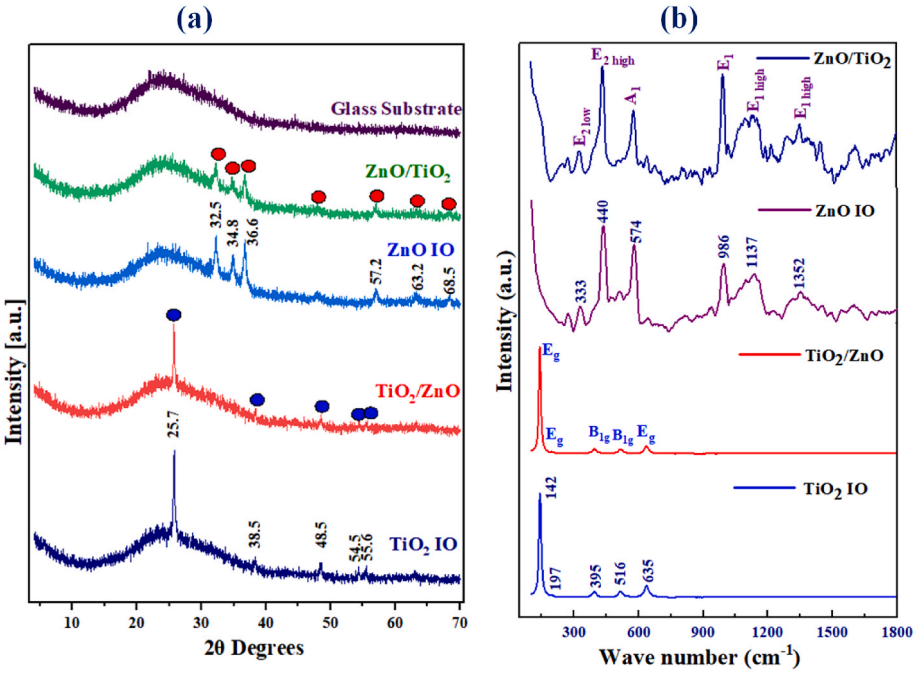

Fig. 5. (a) XRD and (b) Raman results of PEALD IO samples.

The Raman spectrum of the pristine ZnO IO sample revealed several distinctive peaks at 333, 440, 574, 986, 1137, and 1352 cm^{-1}. These peaks could be ascribed to the vibrational modes of the wurtzite ZnO structure, as predicted by group theory (space group $P6_3mc$) [45]. The optic modes of this structure comprised A_1, E_1, $2E_2$, and $2B_1$. The B_1 modes were silent, indicating that they did not participate in Raman scattering [46]. In contrast, the A_1 and E_1 modes were polar, indicating that they could be stimulated by infrared and Raman scattering. The E_2 modes, on the other hand, were nonpolar and only Raman active. The E_2 low mode at 333 cm^{-1} originated from vibrations of Zn atoms in the wurtzite lattice, while the E_2 high mode at 440 cm^{-1} correlated with vibrations of oxygen atoms [47]. The A_1 mode at 574 cm^{-1} and the E_1 mode at 986 cm^{-1} represented stretching and bending vibrations of Zn-O bonds respectively. Finally, the additional peaks at 1137 and 1352 cm^{-1} were assigned to multi-phonon scattering processes involving the E_2 high and E_2 low modes. The most intense and sharp peak in the spectrum, at 440 cm^{-1}, was the intrinsic Raman active mode of ZnO. This mode's presence was a strong suggestion of the wurtzite structure of the ZnO IO sample [48,49].

The Raman spectra of the TiO_2/ZnO and ZiO/TiO_2 composites revealed only the vibrational modes of the dominant, thicker component, indicating that the 10 nm thin layers of TiO_2 and ZnO were too thin to be detected. This observation is consistent with the results obtained from XRD. Additionally, the absence of characteristic carbon peaks in the Raman spectra confirmed the successful removal of the carbon template during the annealing step.

3.6. UV–visible absorbance and reflectance measurement

Fig. 6a and b display the UV–visible absorption and reflectance spectra of the IO materials, respectively. All materials showed enhanced absorption and reflection in the UV region. In Fig. 6a, the pristine TiO_2 IO exhibits a broad absorption band, corresponding to its electric bandgap (E_g = 3.0 eV) shown in Fig. S2 [50]. This is attributed to the size-dependent properties of IO macrostructures. Pores with a size of approximately ~290 nm allow for increased light absorption. The pristine TiO_2 IO exhibits a photonic bandgap (PBG) around 400 and 630 nm (Fig. 6a), which coincides with a reflectance band at 400 and 610 nm (Fig. 6b). This is likely due to the "slow photon" effect, potentially enhancing photocatalytic performance [51]. However, the PBG calculated using Bragg's equation (Table S3) is 394 nm, which matches the experimental values. This can be attributed to the consistent periodicity of the IO macrostructures. Additionally, the PBG is highly influenced by the diameter of the spheres used as templates and the angle of light entering the structure. These opals, characterized by a sphere diameter of 290 nm and wider PBG peaks, exhibit greater polydispersity, which includes variations in pore size [2,34]. The composite TiO_2/ZnO exhibited an absorption spectrum and reflectance spectra identical to the reference TiO_2 inverse opal (Fig. 6a and b). The calculated Bragg's PBG matched that of the reference TiO_2 IO (Table S3). Therefore, the additional PEALD layer on the TiO_2 IO structure did not influence the optical properties of the pure inverse opal.

Pristine ZnO IO exhibits strong light absorption in the UV region, evident from the direct electric band gap (E_g = 3.2 eV) absorption band in Fig. S2. The reflectance peaks at 300, 390, and 470 nm further suggest additional light scattering or reflection within the material (see Fig. 6b). Furthermore, Fig. 6a and b reveal a pronounced peak at 470 nm, a characteristic signature of the "slow light" effect [10]. This exceptional property underscores the potential of ZnO IO material in light manipulation applications [52]. On the other hand, Bragg's equation calculation predicts a PBG around 380 nm (Table S3), which is lower than the experimentally observed 470 nm PBG for ZnO IO (Fig. 6a). This discrepancy highlights potential factors influencing the actual PBG, such as deviations from perfect periodicity in the IO structure or confinement effects due to the material's porosity.

Incorporating an additional 10 nm TiO_2 layer onto the ZnO IO structure (ZnO/TiO_2) significantly improved its optical properties. The absorption spectrum of the composite material exhibited a peak at 500 nm (Fig. 6a) compared to the reference ZnO IO (470 nm). This blue shift, attributed to the enhanced light absorption capabilities induced by the TiO_2 PEALD growth, indicates a shortening of the wavelengths absorbed. While Bragg's calculations predicted a theoretical PBG of 380 nm, a higher value was obtained experimentally. This discrepancy suggests a modification in the lattice structure and light propagation characteristics upon the introduction of the TiO_2 coating. The altered PBG has the potential to expand the range of light manipulation applications for these composite materials [53–55].

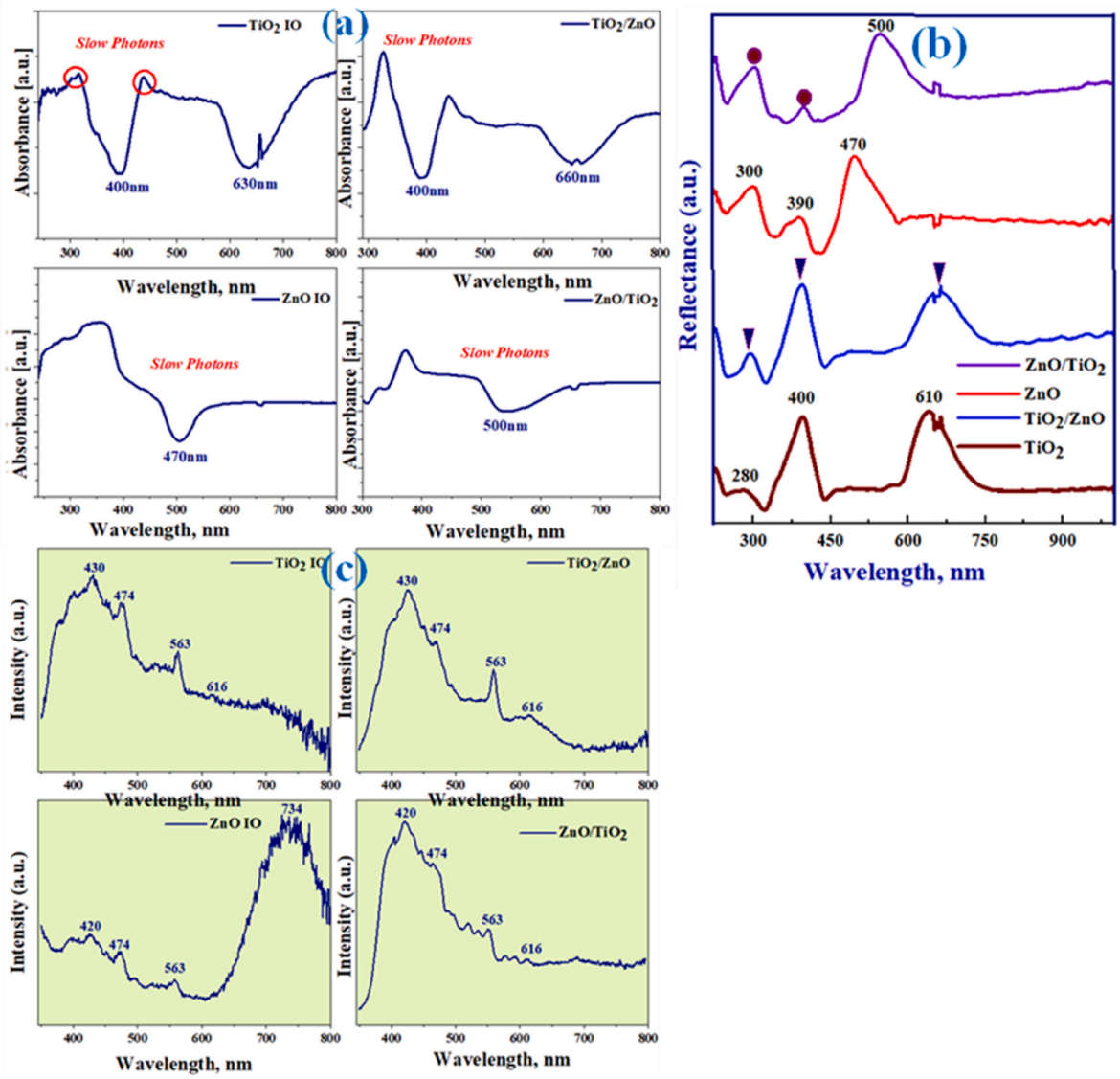

Fig. 6. a) UV Visible absorption spectrum, b) UV Visible Reflectance spectrum, and c) Photoluminescence spectra of the PEALD samples.

3.7. Photoluminescence studies

The study used PL spectroscopy to investigate the optical properties of PEALD-grown IOs made from TiO_2, ZnO, and their composite (TiO_2/ZnO and ZnO/TiO_2) oxides. The results showed that the IOs exhibited PL only in the visible range (Fig. 6c). This is because these materials have an electronic band gap that corresponds to the energy of visible light. When light of this energy is absorbed by the material, electrons are excited from the valence band to the conduction band. These electrons can then recombine with holes in the valence band, releasing energy in the form of light [52,53]. Fig. 6c also shows the pure TiO_2 IO displays a broad emission spectrum with intense peaks in the violet (430 nm), blue (474 nm), and green (563 nm) regions, suggesting multiple recombination pathways for photogenerated electrons and holes [56]. The high intensity indicates the efficient generation of these species, potentially making it a good photocatalyst.

In contrast, the pure ZnO IO exhibits a single strong peak in the blue region (474 nm) with a weaker shoulder peak in the green (563 nm), and red region (734 nm) which is explained by the relaxation of electrons trapped at surface defects [57,58]. The TiO_2/ZnO composite presents a peak in the blue region (474 nm) like the pure materials but with a broader profile. This broadening suggests an interaction between the TiO_2 and ZnO phases, potentially enhancing the charge carrier dynamics which is beneficial for photocatalysis. Similarly, the blue peak (474 nm) with a broader green shoulder indicates that the presence of both TiO_2 and ZnO helps prevent recombination processes compared to pure materials. This improved charge carrier separation can lead to enhanced photocatalytic activity.

3.8. Photocatalytic studies

3.8.1. Degradation of rhodamine 6G and 4-nitrophenol

The photocatalytic activities of Rh6G and 4-NP were investigated using IOs of TiO_2, ZnO, and their composite materials (TiO_2/ZnO and ZnO/TiO_2) under both UV and visible light irradiation. Their efficiencies were evaluated using relative absorbance, calculated according to the following equation:

$$\text{Relative absorbance} = A_t/A_0 \quad (5)$$

Where A_t is the absorbance of the after-irradiation time t, and A_o is the initial absorbance of pollutants.

Both pollutants were effectively degraded by all photocatalysts under both UV and visible light, but degradation rates varied with the photocatalyst and light source.

Under UV light degradation conditions, the pollutants maintained high stability, with relative absorbance values of 0.96 for 4-NP and 0.95 for Rh6G for 4 h, indicating their resistance to UV irradiation. Pristine TiO_2 and ZnO IO samples demonstrated remarkable photocatalytic activity under UV light, surpassing their composite counterparts as shown in Fig. 7 a&c. This superior performance was evidenced by the lower final relative absorbance (A_t/A_o) values of the pollutants, such as 0.41 for 4-NP and 0.51 for Rh6G in pure TiO_2 IO, in comparison to 0.31 for 4-NP and 0.65 for Rh6G in pure ZnO IO, emphasizing the enhanced degradation efficiency. The enhanced photocatalytic efficacy of pristine IO structures in pollutant degradation compared to composite materials stems from their periodically arranged crystal macropore made from a 290 nm sized polystyrene template (the interconnected pores arranged in a periodic lattice create a large surface area, providing more active sites for pollutants molecules to adsorb, facilitating efficient photocatalytic reactions) [59,60], and their electronic band gaps of TiO_2 (3.0 eV) and ZnO (3.2 eV), enabling efficient absorption of UV light photons for pollutants degradation. Furthermore, a closer band gap allows the photocatalyst to absorb UV light photons more efficiently, leading to a greater generation of electron-hole pairs compared to composite counterparts [4]. For example, TiO_2 IO exhibited better degradation of Rh6G compared to pristine ZnO IO, while pristine ZnO IO performed better in degrading 4-NP, respectively.

While the incorporation of a 10 nm PEALD-coated nanocomposite layer onto TiO_2/ZnO or ZnO/TiO_2 IO nanocomposites was intended to improve photocatalysis, it resulted in a decrease in degradation efficiency for both 4NP and Rh6G compared to pristine IOs. This is evidenced by a reduction in relative absorbance value from 0.38/0.42 for TiO_2/ZnO or ZnO/TiO_2 with 4NP and 0.69/0.73 for TiO_2/ZnO or ZnO/TiO_2 with Rh6G (Fig. 7a and c, respectively). These findings suggest that the nanocomposite coating disrupts the optimal light absorption and charge carrier behavior within the IO structure, leading to a general decline in photocatalytic activity. Furthermore, the PEALD coating might introduce defects or interfaces that act as recombination centers for photogenerated charge carriers. These trapped carriers are unable to participate in the photocatalytic process, thus reducing overall efficiency [61–63].

Under visible light irradiation: The 4-NP underwent significant degradation (14 % loss) compared to Rh6G (only 5 % degradation). The 4-NP possesses a nitro group (-NO_2) that acts as an electron acceptor, making it more susceptible to attack by photogenerated radicals during the photocatalytic process [64]. In contrast, Rh6G has a more stable molecular structure, rendering it less reactive towards these radicals [65]. The exceptional photocatalytic performance of these composite IO materials (TiO_2/ZnO and ZnO/TiO_2) in degrading 4-NP/Rh6G pollutants, achieving significant relative absorbance (0.25/0.23 for 4-NP and 0.45/0.55 for Rh6G), can be attributed to a synergistic effect (Fig. 7b and d). Firstly, the combined oxides possess harmonizing bandgaps. This allows for more efficient light absorption across a wider spectrum. Additionally, the interface between ZnO and TiO_2 facilitates improved charge separation, preventing recombination and ultimately leading to increased production of reactive oxygen species responsible for

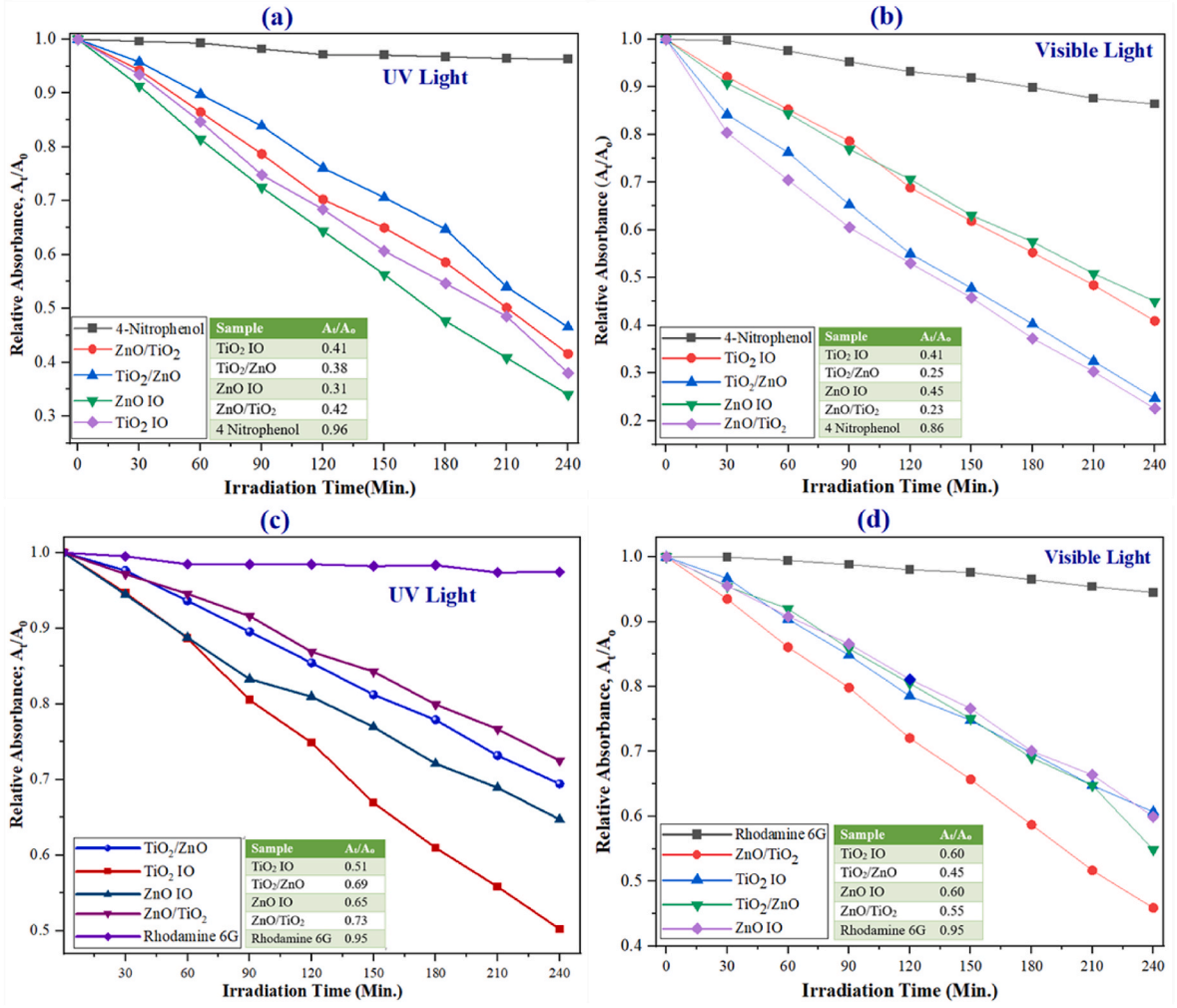

Fig. 7. Photocatalytic degradation of organic pollutants using UV and visible light: (a&b) for 4-nitrophenol and (c&d) for rhodamine 6G respectively.

pollutant degradation [20,66]. Secondly, the periodic interconnected macroporous structure of these composites creates a PBG effect. This PBG acts like a light trap, confining light within the structure and extending its interaction time with the photocatalyst. This extended interaction, known as the "slow photon effect," further enhances light absorption and promotes efficient separation of electron-hole pairs within the material, significantly boosting photocatalytic activity [10, 67,68].

However, pristine IO oxides (TiO_2 and ZnO) exhibit similar, relatively low efficiency (relative absorbance of around 0.60) for Rh6G degradation (Fig. 7d). This can be attributed to two factors: the structure and electronic properties of Rh6G. The bulky aromatic structure of Rh6G may hinder its diffusion within the pores of the photocatalyst, limiting its access to the active sites where degradation occurs. Additionally, the electronic structure of Rh6G might be less susceptible to attack by the photogenerated radicals compared to 4-NP. The presence of the conjugated π-electron system in Rh6G allows for efficient delocalization of the positive charge, making it more challenging for the radicals to break down the molecule [65,69]. In contrast, pristine IO materials (TiO_2 or ZnO) achieve significantly higher relative absorbance for 4-NP degradation (around 0.41 and 0.45, respectively; Fig. 7b). This suggests that the simpler structure of 4-NP enables easier access to the active sites and its electronic configuration makes it more vulnerable to attack by the photogenerated radicals [70].

3.8.2. Photocatalytic degradation rate

A pseudo-first-order equation was used to determine the rate constant of the pollutants degradation in the sample solution:

$$\ln[C_o / C_t] = K_{app} t \quad (6)$$

where k is the rate constant. C_o is the initial concentration of pollutants and C_t is the concentration after irradiation time t. The linear plots of -ln (C_t/C_o) versus irradiation time, t, were shown in (Fig S4 a-d), and the calculated rate constants were provided in Table 1. In this study, all photocatalysts followed pseudo-first-order kinetics. The rate of photodegradation for 4-NP is significantly higher than that for Rh6G under both types of light irradiation after 240 min, observed with all IO photocatalysts. This difference is evident from the K_{app} values for 4-NP, which are consistently higher than those for Rh6G across all light sources. Pristine ZnO IO photocatalyst exhibits a significantly faster rate of 4-NP degradation compared to Rh6G under both UV and visible light irradiation. Specifically, the K_{app} for ZnO IO is 1.9 times faster under UV light and 1.6 times faster under visible light compared to Rh6G. Similarly, pristine TiO_2 IO demonstrated a 1.2 times faster degradation rate for 4-NP ($K_{app} = 0.96$) compared to Rh6G ($K_{app} = 0.78$) under UV light irradiation within 4 h. The composite materials TiO_2/ZnO and ZnO/TiO_2 also showed faster degradation rates for 4-NP than for Rh6G under UV light, as presented in Table 1. Specifically, ZnO/TiO_2 ($K_{app} = 0.88$) and TiO_2/ZnO ($K_{app} = 0.77$) degraded 4-NP more efficiently.

Pristine IOs show faster degradation rates (K_{app}) compared to their composite counterparts likely because of their higher surface area, tunable PBG, slow photon effect, and efficient charge separation making IOs a promising photocatalyst material. The pristine IOs have a highly ordered porous IO structure that enhances the interaction between the photocatalyst and the pollutants, leading to more efficient degradation [71–73]. In contrast, the composites, while still effective, may have slightly less optimal structural properties for light absorption and pollutant interaction, resulting in a marginally slower degradation rate.

Whereas the faster degradation of 4-NP compared to Rh6G can be attributed to the interplay between their chemical structures and light absorption properties. 4-NP's simpler structure, likely lacking the complex conjugated system present in Rh6G (a pollutant molecule), might make it more susceptible to oxidative attack from the photocatalyst, leading to a higher degradation rate. Additionally, the presence of the nitro group in 4-NP broadens its light absorption range to include some visible light, allowing it to take advantage of both UV and visible irradiation for degradation. The interaction of phenolic intermediates with radicals leads to the opening of the aromatic ring, the cleavage of the carbon chain, and eventually mineralization to form CO_2 and H_2O [74,75]. In contrast, Rh6G primarily absorbs in the visible spectrum. While it can still degrade under UV light, the less efficient overlap between its excitation energy and UV light likely leads to a slower degradation rate compared to 4-NP under both light sources.

Visible light enhances the photocatalytic activity of ZnO/TiO_2 and TiO_2/ZnO composite IOs for Rh6G and 4-NP degradation compared to pristine IOs. As shown in Table 1 and Fig S4 b and d, both 4-NP and Rh6G pollutants displayed a higher degradation rate with the ZnO/TiO_2 and TiO_2/ZnO photocatalysts under visible light. Particularly, the 4-NP exhibited a faster degradation rate with the ZnO/TiO_2 composite IOs. For example, the K_{app} for ZnO/TiO_2 with 4-NP was 1.49, while for Rh6G it was 0.78. Similarly, the rate constant for TiO_2/ZnO with 4-NP was 1.39, compared to 0.60 for Rh6G. This is due to visible light effectively excites the composite IOs, creating a synergistic effect between bandgap harmonization and the PBG effect. This enhanced light trapping and improved charge separation significantly boost the generation of reactive oxygen species, leading to faster degradation of 4-NP compared to pristine IOs (due to slightly less optimal structure) and the more robust structure of Rh6G [40,70,76].

3.8.3. The photodegradation mechanism

Photocatalysis leverages light to break down target pollutants. When high-energy light strikes a semiconductor like TiO_2 or ZnO, it excites an electron from the valence band (VB) to the conduction band (CB), creating a hole in the VB. These electron-hole pairs act as powerful oxidizers and reducers, degrading organic molecules adsorbed on the surface of the photocatalysts. The stronger the light energy compared to the semiconductor band gap energy (E_g), the more readily electrons become excited. These excited electrons (e^-) and holes (h^+) then drive degradation through redox reactions [46,56]. For instance, in degrading (Rh6G and 4-NP), light can stimulate pristine IO TiO_2 to generate electron-hole pairs (see schematic diagram in Fig. 8). Electrons can move from ZnO to TiO_2 (oxidation) while holes move from TiO_2 to ZnO (reduction). The holes react with water to produce hydroxyl radicals ($^{\bullet}OH$), potent oxidizers that break down the pollutants into harmless CO_2 and H_2O, while the electrons generate superoxide radicals ($O_2^{-\bullet}$) further contributing to the degradation process (see Fig. 8). This efficient separation of charges by the material interface minimizes recombination and enhances the overall photocatalytic performance [57].

While all PEALD IO photocatalysts exhibited the capability to degrade pollutants under UV light, primarily due to their extensive surface area and the effects of their PBG, the pristine TiO_2 and ZnO IO materials demonstrated superior performance compared to the composite materials (TiO_2/ZnO or ZnO/TiO_2). This enhanced efficiency in pristine TiO_2 and ZnO can be attributed to their more effective electron excitation under UV light exposure (Fig. 8). When UV light interacts with these pristine materials, it excites the electrons more efficiently, leading to the generation of a greater number of reactive radicals. These radicals play a crucial role in the degradation process, breaking down the pollutant molecules more effectively than the composites.

Table: 1
k_{app} of the samples, k_{app} [10^{-2}/min^{-1}].

Sample	UV source	Visible source	Sample	UV source	Visible source
4-NP	0.038	0.14	Rh6G	0.05	0.05
TiO_2 IO	0.96	0.89	TiO_2 IO	0.78	0.51
TiO_2/ ZnO	0.77	1.39	TiO_2/ ZnO	0.50	0.60
ZnO IO	1.07	0.79	ZnO IO	0.56	0.51
ZnO/ TiO_2	0.88	1.49	ZnO/ TiO_2	0.41	0.78

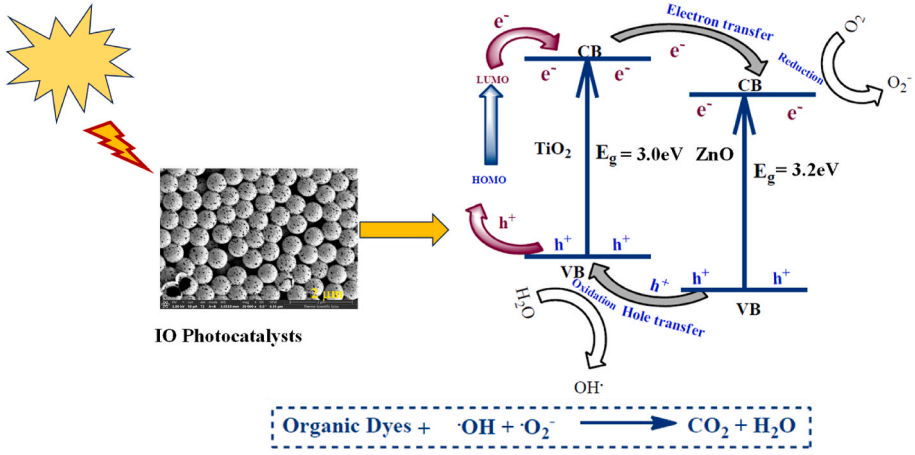

Fig. 8. Schematic representations of photocatalytic materials: PEALD-IOs of TiO_2 and ZnO for degradation of pollutants under UV light irradiation.

Consequently, the higher efficacy of pristine TiO_2 and ZnO in generating these radicals under UV illumination is a key factor in their superior photocatalytic performance.

Composite IO (TiO_2/ZnO and ZnO/TiO_2), demonstrate superior photocatalytic activity compared to pristine TiO_2 or ZnO IOs under visible light irradiation. The visible light with sufficient energy excites electrons within the composite's VB to the CB, creating electron-hole pairs. This h^+ can directly oxidize pollutant molecules (4-NP and Rh6G) adsorbed on the photocatalyst's surface. Alternatively, they can react with water molecules to generate hydroxyl radicals (OH·), even stronger oxidizing agents that degrade the pollutants. Electrons (e^-) in the CB further contribute by reducing molecular oxygen (O_2) to superoxide radicals ($O_2{\cdot}^-$) (refer to Fig. 8). The photocatalytic activity of TiO_2/ZnO and ZnO/TiO_2 IO composites under visible light is significantly enhanced due to several synergistic effects. The key factors contributing to this enhanced performance are as follows:

- The IO photonic crystal structure plays a key role in this enhancement by creating a PBG effect, which effectively traps and guides light within the material. This extended light-matter interaction increases the generation of electron-hole pairs, thereby improving photocatalytic efficiency. Additionally, the unique macrostructure of the IO increases the surface area and enhances adsorption efficiency, offering more active sites for photocatalytic reactions [34,59,77].
- Both TiO_2/ZnO and ZnO/TiO_2 composites have a band gap of approximately 3.2 eV (Fig. S2), making them responsive to visible light. The alignment of the CB and VBs between TiO_2 and ZnO facilitates efficient generation and separation of electron-hole pairs, reducing recombination rates and enhancing photocatalytic activity. This harmonized bandgap enables strong visible light absorption, providing energy to excite electrons, directly degrading pollutants, or generating reactive species like hydroxyl radicals (OH·) and superoxide radicals ($O_2{\cdot}^-$) [20,78].
- Furthermore, the PL spectra of the composite IO showed four major peaks in the visible region (Fig. 6c), with a peak around 420 nm attributed to excitonic PL from oxygen vacancies acting as electron traps. These defects influence PL characteristics and, consequently, photocatalytic performance. The Schottky barrier formed at the TiO_2-ZnO interface in the IO composite further enhances photocatalytic activity by effectively separating photogenerated electron-hole pairs. Electrons accumulate on ZnO, while holes accumulate on TiO_2, prolonging their lifetime and contributing to pollutant degradation. The heterojunction between TiO_2 and ZnO is crucial for creating this Schottky barrier [44,79,80].

Thus, the overall enhancement in photocatalytic performance in these composites results from the combined effects of bandgap harmonization, the PBG effect from the IO structure, efficient charge carrier separation due to the Schottky barrier, and the unique PL properties introduced by surface defects.

4. Conclusion

This study investigated the fabrication of IO photocatalysts of TiO_2, ZnO, and their composites using PEALD at low temperatures in the presence of a sacrificial PS opal template. The results revealed that PEALD enabled the fabrication of high-quality IOs with uniform and conformal coatings. The SEM images revealed the highly ordered and periodic arrangement of monodisperse colloidal spheres in the IOs, resembling close-packed (100) planes of a face-centered cubic (FCC) crystal lattice. EDX analysis confirmed the presence of Ti, Zn, and O elements in the TiO_2, ZnO, and composite IO materials, signifying successful deposition of the desired metal oxides. The XRD and Raman analyses confirmed the successful synthesis of TiO_2, ZnO, and their composite IOs. The XRD patterns showed distinct peaks corresponding to the crystal structures of the individual materials, while the Raman spectra exhibited peaks characteristic of the respective vibrational modes.

UV–Visible absorption and reflectance measurements revealed strong light absorption in the UV region for all IO materials, with the presence of PBGs observed for both TiO_2 and ZnO IO materials. The calculated PBG values using Bragg's equation showed slight discrepancies compared to the experimental values, likely due to variations in the periodicity of the structures. Additionally, incorporating a thin layer of TiO_2 or ZnO onto the composite IO structures resulted in modifications of the absorption and PBG properties. PL spectroscopy revealed visible light emission from all IO materials, indicating the recombination of photogenerated electron-hole pairs, and the emission spectra provided insights into the recombination pathways and potential photocatalytic activities of the materials. The study demonstrates that all photocatalysts followed pseudo-first-order kinetics in degrading pollutants, with significantly higher rates of 4-NP degradation compared to Rh6G under both UV and visible light. This difference is attributed to 4-NP's simpler chemical structure and broader light absorption range. Pristine ZnO IO showed the fastest degradation rates, outperforming both TiO2 IO and their composite counterparts (TiO_2/ZnO and ZnO/TiO_2) due to its higher surface area, and tunable PBG. However, under visible light, composite IOs exhibited superior photocatalytic activity compared to pristine IOs, likely due to bandgap harmonization and enhanced light trapping by the PBG effect. The findings indicate that pristine IO materials are more effective under UV light, while composite IOs excel under visible light, making IOs promising materials for

photocatalytic applications.

CRediT authorship contribution statement

Hamsasew Hankebo Lemago: Writing – review & editing, Writing – original draft, Software, Methodology, Investigation, Formal analysis, Conceptualization. **Letícia Tolezani:** Writing – original draft, Methodology, Formal analysis, Conceptualization. **Tamás Igricz:** Methodology, Investigation, Conceptualization. **Dóra Hessz:** Software, Methodology, Investigation, Formal analysis, Data curation, Conceptualization. **Petra Pál:** Software, Methodology, Investigation, Formal analysis, Data curation, Conceptualization. **Csaba Cserháti:** Resources, Methodology, Investigation, Formal analysis, Data curation, Conceptualization. **Gergő Vecsei:** Methodology, Investigation, Formal analysis, Data curation. **Barbara Sárközi:** Methodology, Investigation, Formal analysis, Data curation. **Eszter Mónika Baradács:** Resources, Methodology, Investigation, Formal analysis, Data curation. **Zoltán Erdélyi:** Writing – review & editing, Software, Resources, Methodology, Formal analysis, Data curation, Conceptualization. **Imre Miklós Szilágyi:** Writing – review & editing, Writing – original draft, Visualization, Supervision, Software, Resources, Methodology, Formal analysis, Conceptualization.

Declaration of interest

The authors have no financial relationships with any companies whose products or services are mentioned in this article. The authors have no patents, trademarks, licensed technologies, or copyrights that could be affected by the publication of this article. The authors have no personal relationships with any individuals whose interests could be affected by the publication of this article.

Acknowledgments

The research conducted at BME and reported in this paper was supported by the NRDI Fund (TKP2021 BME-NVA), which was granted by the NRDI Office under the Ministry for Innovation and Technology. Additionally, project no. TKP2021-NKTA-34 was implemented with the support of the Hungarian National Research, Development, and Innovation Fund (NKFIH) under the grant scheme OTKA K143724 and the TKP2021-NKTA funding scheme. The study was further supported by Stipendium Hungaricum, Hungarian government scholarship.The authors would like to express their gratitude to Budapest University of Technology and Economics, the University of Debrecen, and the Tempus Public Foundation for providing valuable online resources, comprehensive databases, and laboratory facilities.

Appendix A. Supplementary data

Supplementary data to this article can be found online at https://doi.org/10.1016/j.ceramint.2024.10.465.

References

[1] A. Rafiq, M. Ikram, S. Ali, F. Niaz, M. Khan, Q. Khan, M. Maqbool, Photocatalytic degradation of dyes using semiconductor photocatalysts to clean industrial water pollution, J. Ind. Eng. Chem. 97 (2021) 111–128, https://doi.org/10.1016/j.jiec.2021.02.017.

[2] H.M. Yu, J.H. Yim, K.Y. Choi, J.S. Lim, Fabrication and characterization of titania inverse opals using supercritical carbon dioxide, J. Supercrit. Fluids 67 (2012) 71–75, https://doi.org/10.1016/j.supflu.2012.03.005.

[3] D. Qi, L. Lu, Z. Xi, L. Wang, J. Zhang, Enhanced photocatalytic performance of TiO2 based on synergistic effect of Ti3+ self-doping and slow light effect, Appl. Catal. B Environ. 160–161 (2014) 621–628, https://doi.org/10.1016/j.apcatb.2014.06.020.

[4] F. Fathi, M.R. Rashidi, P.S. Pakchin, S. Ahmadi-Kandjani, A. Nikniazi, Photonic crystal based biosensors: emerging inverse opals for biomarker detection, Talanta 221 (2021) 121615, https://doi.org/10.1016/j.talanta.2020.121615.

[5] T. Baba, Slow light in photonic crystals, Nat. Photonics 2 (2008) 465–473, https://doi.org/10.1038/nphoton.2008.146.

[6] E. Armstrong, C. O'Dwyer, Artificial opal photonic crystals and inverse opal structures-fundamentals and applications from optics to energy storage, J. Mater. Chem. C 3 (2015) 6109–6143, https://doi.org/10.1039/c5tc01083g.

[7] X. Huang, Z. Yang, L. Sun, Q. Xie, B. Li, J. Zhou, L. Li, Synthesis and characterization of potassium bismuth titanate inverse opal photonic crystals by sol-gel technique, Mater. Chem. Phys. 114 (2009) 23–25, https://doi.org/10.1016/j.matchemphys.2008.09.074.

[8] J. Hu, S. Yang, Z. Chen, Y. Chen, J. Wei, Inverse opal photonic crystals for real-time identifiable labels via ultraviolet and near-infrared light, ACS Appl. Polym. Mater. (2022), https://doi.org/10.1021/acsapm.2c01933.

[9] E. Armstrong, C. O'Dwyer, Artificial opal photonic crystals and inverse opal structures-fundamentals and applications from optics to energy storage, J. Mater. Chem. C 3 (2015) 6109–6143, https://doi.org/10.1039/c5tc01083g.

[10] J. Liu, J. Jin, Y. Li, H.W. Huang, C. Wang, M. Wu, L.H. Chen, B.L. Su, Tracing the slow photon effect in a ZnO inverse opal film for photocatalytic activity enhancement, J. Mater. Chem. A 2 (2014) 5051–5059, https://doi.org/10.1039/c3ta15044e.

[11] P. Birnal, M.C. Marco de Lucas, I. Pochard, B. Domenichini, L. Imhoff, Photocatalytic properties of atomic layer deposited TiO2 inverse opals and planar films for the degradation of dyes, Appl. Surf. Sci. 512 (2020) 145693, https://doi.org/10.1016/j.apsusc.2020.145693.

[12] H. Chakhtouna, H. Benzeid, N. Zari, A. el kacem Qaiss, R. Bouhfid, Recent progress on Ag/TiO2 photocatalysts: photocatalytic and bactericidal behaviors, Environ. Sci. Pollut. Res. 28 (2021) 44638–44666, https://doi.org/10.1007/s11356-021-14996-y.

[13] S.K. Karuturi, L.J. Liu, L.T. Su, W. Bin Niu, A.L.Y. Tok, Atomic layer deposition of inverse opals for solar cell applications, Adv. Mater. Res. 789 (2013) 3–7. https://doi.org/10.4028/www.scientific.net/AMR.789.3.

[14] J. Long, M. Fu, C. Li, C. Sun, D. He, Y. Wang, High-quality ZnO inverse opals and related heterostructures as photocatalysts produced by atomic layer deposition, Appl. Surf. Sci. 454 (2018) 112–120, https://doi.org/10.1016/j.apsusc.2018.05.160.

[15] M. Chitra, G. Mangamma, K. Uthayarani, N. Neelakandeswari, E.K. Girija, Band gap engineering in ZnO based nanocomposites, Phys. E Low-Dimens. Syst. Nanostruct. 119 (2020) 113969, https://doi.org/10.1016/j.physe.2020.113969.

[16] A. Das, P.M. Kumar, M. Bhagavathiachari, R.G. Nair, Hierarchical ZnO-TiO2 nanoheterojunction: a strategy driven approach to boost the photocatalytic performance through the synergy of improved surface area and interfacial charge transport, Appl. Surf. Sci. 534 (2020) 147321, https://doi.org/10.1016/j.apsusc.2020.147321.

[17] N.S. Zulkiflee, R. Hussin, H. Yahya, Structural and optical characterization of TiO2/ZnO thin films prepared by sol-gel method, Mater. Sci. Forum 888 (MSF) (2017) 290–296. https://doi.org/10.4028/www.scientific.net/MSF.888.290.

[18] F. Bayat, S. Ahmadian Kordasht, A.R. Amani-Ghadim, M. Mohammadnejad, Structural, morphological, and optical analysis of TiO2 inverse opals prepared under different synthesis conditions, Mater. Chem. Phys. 299 (2023), https://doi.org/10.1016/j.matchemphys.2023.127514.

[19] N. Bai, X. Liu, Z. Li, X. Ke, K. Zhang, Q. Wu, High-efficiency TiO2/ZnO nanocomposites photocatalysts by sol–gel and hydrothermal methods, J. Sol. Gel Sci. Technol. 99 (2021) 92–100, https://doi.org/10.1007/s10971-021-05552-8.

[20] K. Gowthaman, P. Gowthaman, M. Venkatachalam, M. Saroja, M. Kutraleeswaran, S. Dhinesh, Design and synthesis of TiO2/ZnO nanocomposite with enhanced oxygen vacancy: better photocatalytic removal of MB dye under visible light-driven condition, Inorg. Chem. Commun. 146 (2022) 110197, https://doi.org/10.1016/j.inoche.2022.110197.

[21] G.K. Upadhyay, J.K. Rajput, T.K. Pathak, V. Kumar, L.P. Purohit, Synthesis of ZnO: TiO2 nanocomposites for photocatalyst application in visible light, Vacuum 160 (2019) 154–163, https://doi.org/10.1016/j.vacuum.2018.11.026.

[22] J. Pandele-Cusu, S. Petrescu, S. Preda, G. Petcu, M. Ciobanu, L. Predoana, Comparative study of the TiO2 nanopowders prepared from different precursors and chemical methods for heterogeneous photocatalysis application, J. Therm. Anal. Calorim. 147 (2022) 13111–13124, https://doi.org/10.1007/s10973-022-11544-9.

[23] K. Zhou, P. Li, Y. Zhu, X. Ye, H. Chen, Y. Yang, Y. Dan, Y. Yuan, H. Hou, Atomic layer deposition of ZnO on TiO2 nanofibers for boosted photocatalytic hydrogen production, Catal. Lett. 151 (2021) 78–85, https://doi.org/10.1007/s10562-020-03276-y.

[24] C. Foo, Y. Li, K. Lebedev, T. Chen, S. Day, C. Tang, S.C.E. Tsang, Characterisation of oxygen defects and nitrogen impurities in TiO2 photocatalysts using variable-temperature X-ray powder diffraction, Nat. Commun. 12 (2021) 1–13, https://doi.org/10.1038/s41467-021-20977-z.

[25] R. Nadarajan, W.A. Wan Abu Bakar, R. Ali, R. Ismail, Effect of structural defects towards the performance of TiO2/SnO2/WO3 photocatalyst in the degradation of 1,2-dichlorobenzene, J. Taiwan Inst. Chem. Eng. 64 (2016) 106–115, https://doi.org/10.1016/j.jtice.2016.03.044.

[26] R.W. Johnson, A. Hultqvist, S.F. Bent, A brief review of atomic layer deposition: from fundamentals to applications, Mater. Today 17 (2014) 236–246, https://doi.org/10.1016/j.mattod.2014.04.026.

[27] J.R. Castillo-Saenz, N. Nedev, B. Valdez-Salas, M.A. Martinez-Puente, F.S. Aguirre-Tostado, M.I. Mendivil-Palma, D. Mateos, M.A. Curiel-Alvarez, O. Perez-Landeros, E. Martinez-Guerra, Growth of ZnO thin films at low temperature by plasma-enhanced atomic layer deposition using H2O and O2 plasma oxidants, J. Mater. Sci. Mater. Electron. 32 (2021) 20274–20283, https://doi.org/10.1007/s10854-021-06533-x.

[28] R. Lo Nigro, E. Schilirò, G. Mannino, S. Di Franco, F. Roccaforte, Comparison between thermal and plasma enhanced atomic layer deposition processes for the

growth of HfO2 dielectric layers, J. Cryst. Growth 539 (2020) 125624, https://doi.org/10.1016/j.jcrysgro.2020.125624.
[29] E. Langereis, M. Bouman, J. Keijmel, M.C. Van de Sanden, W.M. Kessels, Plasma-assisted ALD of Al2O3 at low temperatures: reaction mechanisms and material properties, ECS Meet. Abstr MA2008–02 (2008) 1914, https://doi.org/10.1149/ma2008-02/24/1914, 1914.
[30] S.B.S. Heil, J.L. Van Hemmen, M.C.M. Van De Sanden, W.M.M. Kessels, Reaction mechanisms during plasma-assisted atomic layer deposition of metal oxides: a case study for Al2O3, J. Appl. Phys. 103 (2008), https://doi.org/10.1063/1.2924406.
[31] C. Detavernier, D. Deduytsche, J. Musschoot, J. Dendooven, Thermal versus plasma-enhanced ALD: growth kinetics and conformality, ECS Meet. Abstr. MA2008–02 (2008) 1913, https://doi.org/10.1149/ma2008-02/24/1913, 1913.
[32] H. Lemago, N. Khauli, D. Hessz, T. Igricz, P. Petra, Fabrication of ZnO-Al 2 O 3 Inverse Opals with Atomic Layer Deposited Amorphous - Al 2 O 3 for Enhanced Photocatalysis, Mater. Sci. Semicond. Process. 183 (2024) 1–33, https://doi.org/10.1016/j.mssp.2024.108733.
[33] H.H. Lemago, F.S. Addin, K. Atilla, B. Parditka, D. Hessz, I. Mikl, Synthesis of TiO 2/Al 2 O 3 Double-Layer Inverse Opal by Thermal and Plasma-Assisted Atomic Layer Deposition for Photocatalytic Applications, Nanomater. 13 (8) (2023) 1314. https://doi.org/10.3390/nano13081314.
[34] G.I.N. Waterhouse, M.R. Waterland, Opal and inverse opal photonic crystals: fabrication and characterization, Polyhedron 26 (2007) 356–368, https://doi.org/10.1016/j.poly.2006.06.024.
[35] C.J. Summers, E. Graugnard, D.P. Gaillot, J.S. King, Luminescent and tunable 3D photonic crystal structures, J. Nonlinear Opt. Phys. Mater. 15 (2006) 203–218, https://doi.org/10.1142/S0218863506003207.
[36] J.B. Coulter, D.P. Birnie, Assessing Tauc plot slope quantification: ZnO thin films as a model system, Phys. Status Solidi Basic Res. 255 (2018) 1–7, https://doi.org/10.1002/pssb.201700393.
[37] Y. Wang, Y. Dai, H. Tüysüz, Preparation and properties of polystyrene nanospheres incorporated Cs3Bi2Br9 halide perovskite disks, Eur. J. Inorg. Chem. 2021 (2021) 2712–2717, https://doi.org/10.1002/ejic.202100338.
[38] J. Liu, X. Zhang, W. Li, C. Jiang, Z. Wang, X. Xiao, Recent progress in periodic patterning fabricated by self-assembly of colloidal spheres for optical applications, Sci. China Mater. 63 (2020) 1418–1437, https://doi.org/10.1007/s40843-020-1284-8.
[39] H.K.E. Latha, H.S. Lalithamba, Synthesis and characterization of titanium dioxide thin film for sensor applications, Mater. Res. Express 5 (2018), https://doi.org/10.1088/2053-1591/aab695.
[40] M.M. Ali, M.J. Haque, M.H. Kabir, M.A. Kaiyum, M.S. Rahman, Nano synthesis of ZnO–TiO2 composites by sol-gel method and evaluation of their antibacterial, optical and photocatalytic activities, Results Mater 11 (2021) 100199, https://doi.org/10.1016/j.rinma.2021.100199.
[41] M.C. Uribe-López, M.C. Hidalgo-López, R. López-González, D.M. Frías-Márquez, G. Núñez-Nogueira, D. Hernández-Castillo, M.A. Alvarez-Lemus, Photocatalytic activity of ZnO nanoparticles and the role of the synthesis method on their physical and chemical properties, J. Photochem. Photobiol. Chem. 404 (2021), https://doi.org/10.1016/j.jphotochem.2020.112866.
[42] M.J. Šćepanović, M.U. Grujić-Brojčin, Z.D. Dohčević-Mitrović, Z.V. Popović, Effects of confinement, strain and nonstoichiometry on Raman spectra of anatase TiO2 nanopowders, Mater. Sci. Forum 518 (2006) 101–106. https://doi.org/10.4028/www.scientific.net/MSF.518.101.
[43] X.M. Liu, W.L. Zhong, Y.C. Huang, G.S. Zhang, X.K. Bai, X.C. Wei, C.X. Lei, Facile preparation of spherical TiO2 inverse opals with enhanced visible-light photodegradation of methylene blue, J. Mater. Sci. Mater. Electron. 32 (2021) 21742–21755, https://doi.org/10.1007/s10854-021-06694-9.
[44] Y. Wan, J. Wang, X. Wang, H. Xu, S. Yuan, Q. Zhang, M. Zhang, Preparation of inverse opal titanium dioxide for photocatalytic performance research, Opt. Mater. 96 (2019) 109287, https://doi.org/10.1016/j.optmat.2019.109287.
[45] J.R. Lombardi, R.L. Birke, Theory of surface-enhanced Raman scattering in semiconductors, J. Phys. Chem. C 118 (2014) 11120–11130, https://doi.org/10.1021/jp5020675.
[46] N. Romević, R. Kostić, B. Hadić, M. Romević, I. Kuryliszyn-Kudelska, W. D. Dobrowolski, U. Narkiewicz, D. Sibera, Raman scattering from ZnO incorporating Fe nanoparticles: vibrational modes and low-frequency acoustic modes, J. Alloys Compd. 507 (2010) 386–390, https://doi.org/10.1016/j.jallcom.2010.08.013.
[47] A.G. Milekhin, N.A. Yeryukov, L.L. Sveshnikova, T.A. Duda, E.I. Zenkevich, S. S. Kosolobov, A.V. Latyshev, C. Himcinski, N.V. Surovtsev, S.V. Adichtchev, Z. C. Feng, C.C. Wu, D.S. Wuu, D.R.T. Zahn, Surface enhanced Raman scattering of light by ZnO nanostructures, J. Exp. Theor. Phys. 113 (2011) 983–991, https://doi.org/10.1134/S1063776111140184.
[48] R. Cuscó, E. Alarcón-Lladó, J. Ibáñez, L. Artús, J. Jiménez, B. Wang, M.J. Callahan, Temperature dependence of Raman scattering in ZnO, Phys. Rev. B Condens. Matter 75 (2007) 1–11, https://doi.org/10.1103/PhysRevB.75.165202.
[49] P. Sharma, V.S. Bhati, M. Kumar, R. Sharma, R. Mukhiya, K. Awasthi, M. Kumar, Development of ZnO nanostructure film for pH sensing application, Appl. Phys. Mater. Sci. Process 126 (2020) 1–7, https://doi.org/10.1007/s00339-020-03466-w.
[50] A.R. Zanatta, Revisiting the optical bandgap of semiconductors and the proposal of a unified methodology to its determination, Sci. Rep. 9 (2019) 11225, https://doi.org/10.1038/s41598-019-47670-y.
[51] Z. Geng, Y. Yu, J. Liu, Broadband plasmonic photocatalysis enhanced by photothermal light absorbers, J. Phys. Chem. C 127 (2023) 17723–17731, https://doi.org/10.1021/acs.jpcc.3c03639.
[52] D. Karajz, D. Cseh, B. Parditka, Z. Erdélyi, I. Szilágyi, Combining ZnO inverse opal and ZnO nanorods using ALD and hydrothermal growth, J. Therm. Anal. Calorim. (2022), https://doi.org/10.1007/s10973-022-11255-1.
[53] C. Yang, Q. Li, ZnO inverse opals with deposited Ag nanoparticles: fabrication, characterization and photocatalytic activity under visible light irradiation, J. Photochem. Photobiol. Chem. 371 (2019) 118–127, https://doi.org/10.1016/j.jphotochem.2018.10.039.
[54] X. Wu, D. Lan, R. Zhang, F. Pang, J. Ge, Fabrication of opaline ZnO photonic crystal film and its slow-photon effect on photoreduction of carbon dioxide, Langmuir 35 (2019) 194–202, https://doi.org/10.1021/acs.langmuir.8b03327.
[55] J. Pilz, A. Perrotta, G. Leising, A.M. Coclite, ZnO thin films grown by plasma-enhanced atomic layer deposition: material properties within and outside the “atomic layer deposition window,”, Phys. Status Solidi Appl. Mater. Sci. 217 (2020) 1–8, https://doi.org/10.1002/pssa.201900256.
[56] A. Saha, A. Moya, A. Kahnt, D. Iglesias, S. Marchesan, R. Wannemacher, M. Prato, J.J. Vilatela, D.M. Guldi, Interfacial charge transfer in functionalized multi-walled carbon nanotube@TiO2 nanofibres, Nanoscale 9 (2017) 7911–7921, https://doi.org/10.1039/c7nr00759k.
[57] H. Noh, M. Scharrer, M.A. Anderson, R.P.H. Chang, H. Cao, Photoluminescence modification by a high-order photonic band with abnormal dispersion in ZnO inverse opal, Phys. Rev. B Condens. Matter 77 (2008) 1–9, https://doi.org/10.1103/PhysRevB.77.115136.
[58] O.K.M. Bashiar, R.E. Kroon, H.C. Swart, R.A. Harris, Producing ZnO films that exhibited near-infrared (NIR) luminescence with a templated design procedure, Phys. B Condens. Matter 673 (2024) 415523, https://doi.org/10.1016/j.physb.2023.415523.
[59] J. Yu, J. Lei, L. Wang, J. Zhang, Y. Liu, TiO2 inverse opal photonic crystals: synthesis, modification, and applications - a review, J. Alloys Compd. 769 (2018) 740–757, https://doi.org/10.1016/j.jallcom.2018.07.357.
[60] L.P. Bakos, D. Karajz, A. Katona, K. Hernadi, B. Parditka, Z. Erdélyi, I. Lukács, Z. Hórvölgyi, G. Szitási, I.M. Szilágyi, Carbon nanosphere templates for the preparation of inverse opal titania photonic crystals by atomic layer deposition, Appl. Surf. Sci. 504 (2020), https://doi.org/10.1016/j.apsusc.2019.144443.
[61] S. Bai, N. Zhang, C. Gao, Y. Xiong, Defect engineering in photocatalytic materials, Nano Energy 53 (2018) 296–336, https://doi.org/10.1016/j.nanoen.2018.08.058.
[62] C.A. Aggelopoulos, M. Dimitropoulos, A. Govatsi, L. Sygellou, C.D. Tsakiroglou, S. N. Yannopoulos, Influence of the surface-to-bulk defects ratio of ZnO and TiO2on their UV-mediated photocatalytic activity, Appl. Catal. B Environ. 205 (2017) 292–301, https://doi.org/10.1016/j.apcatb.2016.12.023.
[63] Y. Heo, S.Y. Lee, J.W. Kim, T.Y. Jeon, S.H. Kim, Controlled insertion of planar defect in inverse opals for anticounterfeiting applications, ACS Appl. Mater. Interfaces 9 (2017) 43098–43104, https://doi.org/10.1021/acsami.7b13946.
[64] B. Anusha, M. Anbuchezhiyan, C. Deepa, N. Srinivasan alias Arunsankar, Novel approaches to the degradation of nitrophenols using TiO2-biopolymer-ligand-metal complex as photocatalysts, J. Mater. Sci. Mater. Electron. 35 (2024) 1–17, https://doi.org/10.1007/s10854-024-12323-y.
[65] A.V. Mohod, M. Momotko, N.S. Shah, M. Marchel, M. Imran, L. Kong, G. Boczkaj, Degradation of rhodamine dyes by advanced oxidation processes (AOPs) – focus on cavitation and photocatalysis - a critical review, Water Resour. Ind. 30 (2023), https://doi.org/10.1016/j.wri.2023.100220.
[66] K. Hasibur, A. Kumar, K. Chen, Materials Science & Engineering B Highly active ZnO/Fe 3 + -TiO 2 photocatalysts for visible-light photodegradation application and its colour change behaviour by d-d transition, Mater. Sci. Eng. B 305 (2024) 117394, https://doi.org/10.1016/j.mseb.2024.117394.
[67] X. Zhang, S. John, Enhanced photocatalysis by light-trapping optimization in inverse opals, J. Mater. Chem. A 8 (2020) 18974–18986, https://doi.org/10.1039/d0ta05655c.
[68] J. Ginter, I. Piwoński, Evaluation of the synergistic effect between slow photons and electron trapping on the photocatalytic properties of TiO2 photonic crystals, Mater. Res. Bull. 107 (2018) 100–110, https://doi.org/10.1016/j.materresbull.2018.07.010.
[69] N.B. Bokhale, S.D. Bomble, R.R. Dalbhanjan, D.D. Mahale, S.P. Hinge, B. S. Banerjee, A.V. Mohod, P.R. Gogate, Sonocatalytic and sonophotocatalytic degradation of rhodamine 6G containing wastewaters, Ultrason. Sonochem. 21 (2014) 1797–1804, https://doi.org/10.1016/j.ultsonch.2014.03.022.
[70] H.G. Lee, G. Sai-Anand, S. Komathi, A.I. Gopalan, S.W. Kang, K.P. Lee, Efficient visible-light-driven photocatalytic degradation of nitrophenol by using graphene-encapsulated TiO2 nanowires, J. Hazard Mater. 283 (2015) 400–409, https://doi.org/10.1016/j.jhazmat.2014.09.014.
[71] S. Meng, D. Li, P. Wang, X. Zheng, J. Wang, J. Chen, J. Fang, X. Fu, Probing photonic effect on photocatalytic degradation of dyes based on 3D inverse opal ZnO photonic crystal, RSC Adv. 3 (2013) 17021–17028, https://doi.org/10.1039/c3ra42618a.
[72] J. Gao, W. Tian, H. Zhang, S. Wang, Engineered inverse opal structured semiconductors for solar light-driven environmental catalysis, Nanoscale (2022) 14341–14367, https://doi.org/10.1039/d2nr03924a.
[73] L. Liu, S.K. Karuturi, L.T. Su, A.I.Y. Tok, TiO2 inverse-opal electrode fabricated by atomic layer deposition for dye-sensitized solar cell applications, Energy Environ. Sci. 4 (2011) 209–215, https://doi.org/10.1039/c0ee00086h.
[74] D.B. Thinh, N.T. Tien, N.M. Dat, H.H.T. Phong, N. Thi Huong Giang, L.T. Tai, D. Thi Yen Oanh, H.M. Nam, M.T. Phong, N.H. Hieu, Improved photodegradation of p-nitrophenol from water media using ternary MgFe2O4-doped TiO2/reduced graphene oxide, Synth. Met. 270 (2020) 116583, https://doi.org/10.1016/j.synthmet.2020.116583.
[75] N. Wang, G. Lv, L. He, X. Sun, New insight into photodegradation mechanisms, kinetics and health effects of p-nitrophenol by ozonation in polluted water,

J. Hazard Mater. 403 (2021) 123805, https://doi.org/10.1016/j.jhazmat.2020.123805.

[76] Y. zhen Dong, Y. shan Xue, W. wei Yang, H. ming You, Y. Su, Visible light driven CdS/WO3 inverse opals with enhanced RhB degradation activity, Colloid. Surf. A Physicochem. Eng. Asp. 561 (2019) 381–387, https://doi.org/10.1016/j.colsurfa.2018.10.033.

[77] V. Likodimos, Photonic crystal-assisted visible light activated TiO2 photocatalysis, Appl. Catal. B Environ. 230 (2018) 269–303, https://doi.org/10.1016/j.apcatb.2018.02.039.

[78] P. Akhter, S. Nawaz, I. Shafiq, A. Nazir, S. Shafique, F. Jamil, Y.K. Park, M. Hussain, Efficient visible light assisted photocatalysis using ZnO/TiO2 nanocomposites, Mol. Catal. 535 (2023) 112896, https://doi.org/10.1016/j.mcat.2022.112896.

[79] M. Tahir, S. Tasleem, B. Tahir, Recent development in band engineering of binary semiconductor materials for solar driven photocatalytic hydrogen production, Int. J. Hydrogen Energy 45 (2020) 15985–16038, https://doi.org/10.1016/j.ijhydene.2020.04.071.

[80] H. Khan, M.U.H. Shah, Modification strategies of TiO2 based photocatalysts for enhanced visible light activity and energy storage ability: a review, J. Environ. Chem. Eng. 11 (2023), https://doi.org/10.1016/j.jece.2023.111532.